Phase transitions in crystalline materials

Jun Li

Department of Mechanical Science and Engineering
University of Illinois Urbana Champaign

Abstract

We reviewed structural phase transitions in crystalline materials, especially recent simulations and experiments on the shock-induced transitions in iron. They both confirmed a phase transition wave in the picosecond to nanosecond time scale, inferred previously from wave profile analyses. The nonequilibrium molecular dynamics simulation suggests modification of pair potentials from temperature-induced to shock-induced transitions. The x-ray diffraction measurements are consistent with a compression and shuffle mechanism and in good agreement with simulation results.

1 Introduction

Crystalline materials are ubiquitous both in nature and industry. One of their fundamental properties is seen from the crystallographic structure. It is well known that the material may change its crystal structure abruptly when the temperature or pressure varies, resulting in a discontinuous change in material properties. Typically in steel, the structural transition was widely used to enhance strength by fast cooling long time ago. Another application is the shape-memory effect in some alloys and widely used in medical devices. It is also observed in biological systems, such as some virus use the pressure-induced structural transitions to infect bacteria cells [1].

The crystalline phase transition, also known as the Martensitic phase transition, is a diffusionless, solid-to-solid phase transition where the lattice or molecular structure changes. Figure 1 illustrates this process schematically. At the beginning of a high temperature phase, the atoms are arranged in a square lattice as shown in Fig.1 (a), the Austenite phase. If it is cooled and reaches a critical temperature, the

arrangement changes abruptly to a rectangular lattice shown in Fig.1 (b), the Martensite phase. We can see that the Austenite phase has grater crystallographic symmetry than that of the Martensite phase. Typically we have multiple symmetry-related variants of Martensite. For example, the square lattice in Fig.1 (a) can transform to the rectangular lattice in Fig. 1 (c) instead of in Fig.1 (b). Indeed, different regions of a crystal may transform to different variants and form different shapes due to applied loads as shown in Fig. 1 (d). While if we heat the crystal to a critical temperature, it would abruptly change back to the original square lattice with one possible shape (no variants). This process is reversible and also explains the shape-memory effect. In contrast, the Martensitic transformation is not reversible in some materials like steels or CoNi. These are characterized by significant dislocations and twinning in the parent phase. The reversibility has recently been explained elegantly by Bhattacharya et al. [2] in terms of the symmetry groups of the parent and the product phases.

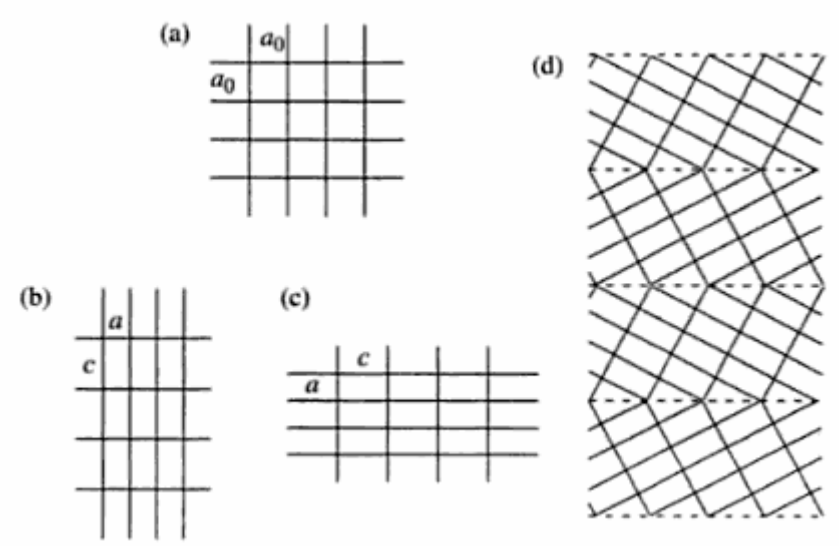

Fig. 1: An illustration of the martensitic phase transformation, adapted from Bhattacharya [1]. (a) austenite (b, c) variants of martensite and (d) arrangement of alternating variants of martensite.

The Martensitic transformation has distinguished features from conventional phase transitions in the following sense: 1) the coexistence of two phases over a wide temperature and pressure range; 2) the non-ergodicity resulting in path-dependent

equilibrium microstructure and related hysteresis; 3) pressure-induced transition and shape memory effect; 4) unique morphological patterns of internally twinned plates. Many open questions remain in understanding the mechanism of this transition.

In this paper we focus on shock-induced structural phase transitions in iron, especially recent simulations by Kadau et al. [3,4] and experiments by Kalantar et al. [5,6]. Iron has a ferromagnetic body-centered cubic (bcc) ground state (α-Fe), and the nonmagnetic hexagonal close-packed (hcp) phase (ε-Fe) in a pressure-induced transition at room temperature and 13 GPa. At the triple point of about 800 K and 10.5 GPa, the antiferromagnetic face-centered cubic (fcc) γ-Fe phase appears. The $\alpha \to \varepsilon$ transition was inferred previously from the correlation between shock-wave profile analyses and static high-pressure x-ray measurements, while Kalantar et al.'s experiments provide first direct observation during the shock loading time scale (nanoseconds). It also confirmed a compression and shuffle mechanism for the phase transition by analyzing x-ray diffraction images. The large-scale nonequilibrium molecular dynamics simulations by Kadau at al. can possibly understand the physics at the atomic level and help to interpret experiments within the shock loading process. They used two embedded atom method potentials to simulation the process. In order to be consistent with experimental data, they found one must change potential models from temperature-induced to shock-induced transitions.

2 Methods

Kadau et al. [3,4] used non-equilibrium molecular dynamics (NEMD) to simulate shock-induced structural phase transitions. The simulation is based on embedded atom method (EAM) potentials to describe interaction between atoms. This model is particularly appropriate for metal and semiconductor systems. The potential energy of a system of N equal atoms gives

$$E = \sum_{i}^{N} F\left(\rho_i\right) + \sum_{i<j}^{N} \phi\left(r_{ij}\right), \tag{1}$$

where r_{ij} is the distance between atoms i and j, ϕ is a pair-wise potential, F

represents the embedding energy to place atom i into the electron cloud, which depends on the background electronic density,

$$\rho_i = \sum_{i \neq j}^{N} \rho_j^{at}\left(r_{ij}\right). \tag{2}$$

In the simulation two different empirical EAM potentials are employed: the Voter-Chen (VC) potential and the Meyer-Entel (ME) force-field. Both potentials accurately reproduce the lattice constant, cohesive energy, elastic properties, and the vacancy energy of bcc Fe. In addition, the ME potential was fit to zone-boundary phonon frequencies that are particular important in describing temperature-driven Martensitic transformations. While the VC potential used the empirical Rose equation of state and fit well to the ferromagnetic ground state of bcc Fe. Their results would be compared to available experimental data to see the accuracy.

The system is composed of about N=1 million to 8 million atoms and the length in the shock direction from about 60 nm to 1 μm. Shock waves were initiated by slamming the sample up against a specularly reflecting wall at piston (or particle) velocity u_p (the so-called "momentum mirror" method). The velocity of resulting shock wave moving in front of the piston is identified as u_s. Periodic boundary conditions perpendicular to the shock direction are applied to minimize edge effects and simulate a pseudoinfinite lateral dimension. For clarity and brevity shock waves were generated in the [001] direction. The regions of bcc, uniaxially compressed bcc, grain boundaries, and the close-packed phase are identified by counting the neighbors n for each atom within 2.75 Å: bcc (n=8), uniaxially compressed bcc (n=10), grain boundaries (n=11), close-packed (n=12).

Kalantar et al. [5,6] used the technique of wide-angle, in situ diffraction to observe the structural phase transitions. They prepared samples of 200 μm thick single crystal [001] iron coated with a 16–20 μm parylene-*N* ablator layer and followed by a 0.1 μm aluminum shine-through layer. Iron K-shell x rays with a wavelength of 1.85 Å were created by direct irradiation of an iron foil positioned 1.3

mm from the shocked crystal sample. The setup is shown up in Fig. 2.

Shock loadings were generated by direct laser irradiation at 2×10^{10} to $1\times10^{12} W/cm^2$ with 2–6ns constant intensity laser pulses. The x rays are incident on the crystal at a wide angle and diffracted from many different lattice planes in the crystal, resulting in line features on the film. The $\alpha \rightarrow \varepsilon$ transition can be observed and measured from x-ray diffraction images.

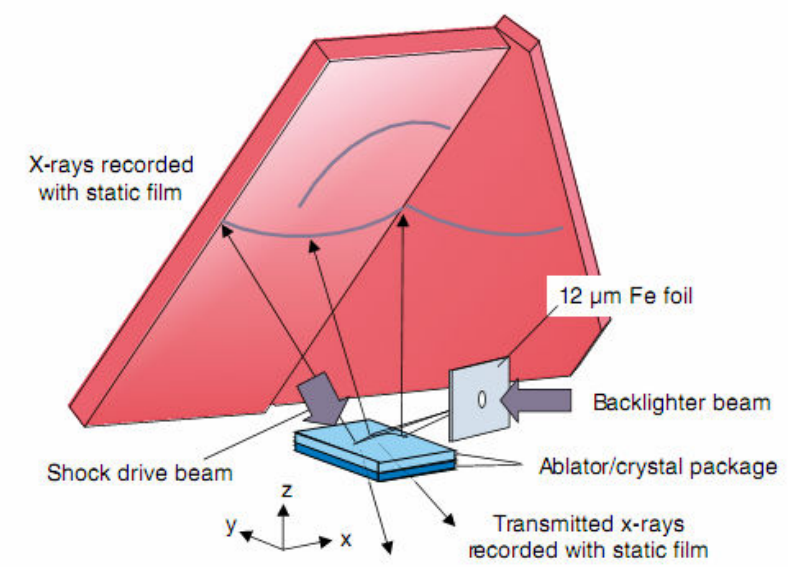

Fig. 2: Experimental setup in Kalantar *et al.* [5] for *in situ* wide-angle diffraction measurements.

3. Results and discussion

Kadau et al. simulated shock waves in the system by varying initial shock strength. The results of final states at 8.76ps are shown in Fig. 3. For low particle velocities, an elastic shock wave of uniaxially compressed bcc was observed in Fig. 3(a). With increasing shock strength from Fig. 3 (b) to (d), a two-wave shock structure was identified in Fig. 3 (b) and (c), with an elastic precursor followed by a slower phase-transition wave. The transition is induced by thermal fluctuations (homogeneous nucleation) or preexisting defects (heterogeneous nucleation). Assuming perfect single crystal in the simulation, homogeneous nucleation of hcp grains was observed through out. Near the threshold (Fig. 3 b), the transition front is rough since only a few nuclei appear and establish the front. As the shock strength

increases, a smoother transition front is observed, while at very high loading (Fig. 3 d), this front overtakes the elastic precursor, resulting in a single overdriven wave.

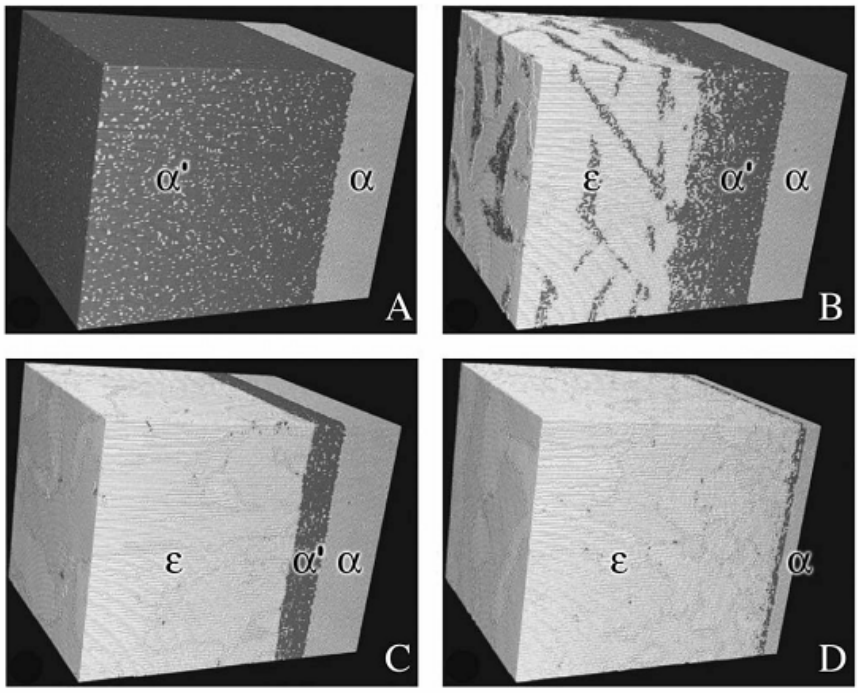

Fig. 3 Representations of NEMD simulation for the four cases with increasing shock strength, where the color coding corresponds to different phases: gray- uncompressed bcc, dark gray- uniaxially compressed bcc, and light gray- hcp, reproduced from Kadau et al. [3].

The resulting shock velocity u_s for various particle velocities u_p was shown in Fig. 4 (a) (two velocities when the two-wave structure exists). The pressure-volume relationship is deduced by conservation of mass and momentum across the shock front, which relates the initial (subscript 0) and final states (jump conditions):

$$V / V_0 = 1 - u_p / u_s, \tag{3}$$

$$P - P_0 = u_s u_p / V_0. \tag{4}$$

It is noted that results for the two potentials demonstrate same qualitative behavior while quantitatively different. For the Voter-Chen potential, the transition pressure of 15 GPa agrees well with previous experimental 13 GPa (Brown et al. [7]) (Fig. 4 b). While the Meyer-Entel potential is much too repulsive with a high transition pressure of 55 GPa. We note that the ME potential fit well in temperature-induced phase transitions while the VC potential does not. It follows that

an EAM potential that well reproduced both the temperature-driven and the pressure-driven phase transitions does not apply for an element like Fe. One should be cautious to choose a description depending on the questions asked. We may need a modified embedded-atom method for a more global description of the iron phase transitions.

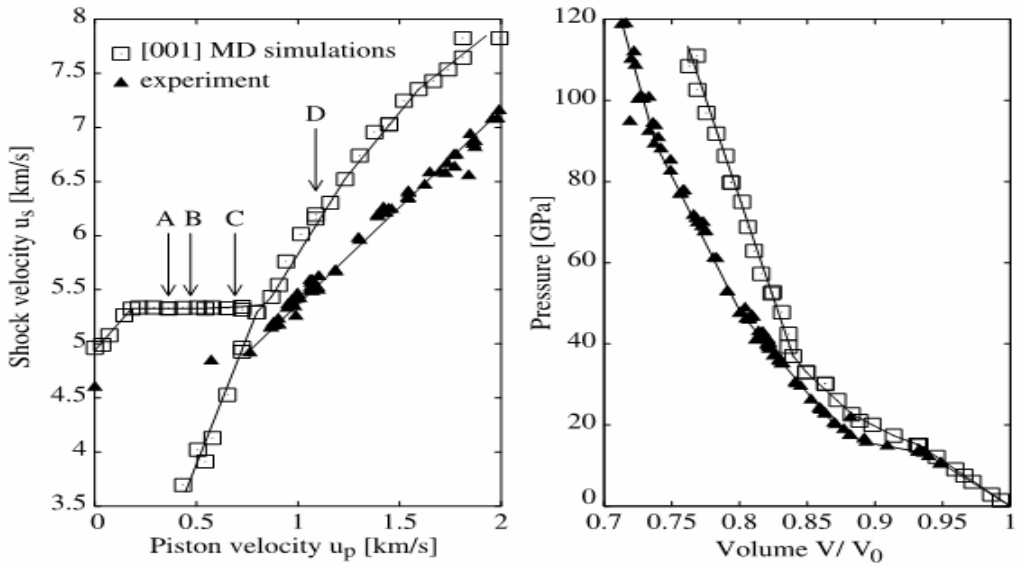

Fig. 4: Shock velocities as a function of particle velocities and the corresponding pressure-volume relationship obtained from the jump conditions. The letters A, B, C, and D correspond to the snapshots shown in Fig. 3. The interatomic pair potentials were prescribed by a Voter-Chen EAM potential, showing good agreement with previous experiments by Brown et al. [7].

Kalantar et al. analyzed their experiments from sample x-ray diffraction images. Three of them are shown in Fig. 5, where the first two show x rays in reflection geometry with a low intensity laser drive (Fig. 5 a) and a high intensity laser drive (Fig. 5 b), and the third (Fig. 5 c) recorded a high intensity laser drive in transmission geometry. A high intensity laser drive is related to a high shock pressure. In Fig. 5(a) we see shifts of green diffraction lines, consistent with uniaxial compression motion at low shock pressure. Fig. 5(b) shows multiple compression regions with green and red dashed overlays. The green shifted lines referred to a compression of approximately 6% and the red diffuse lines indicated compression by 15%-18%, clearly demonstrated a transition to the hcp phase. The diffuse lines in transmission diffraction images (Fig. 5 c) also indicated presence of hcp phases. The observation of

a collapse along the shock direction (001) and the shuffling of alternate (110) planes is consistent with the compression and shuffle mechanism described by Wang and Ingalls [8].

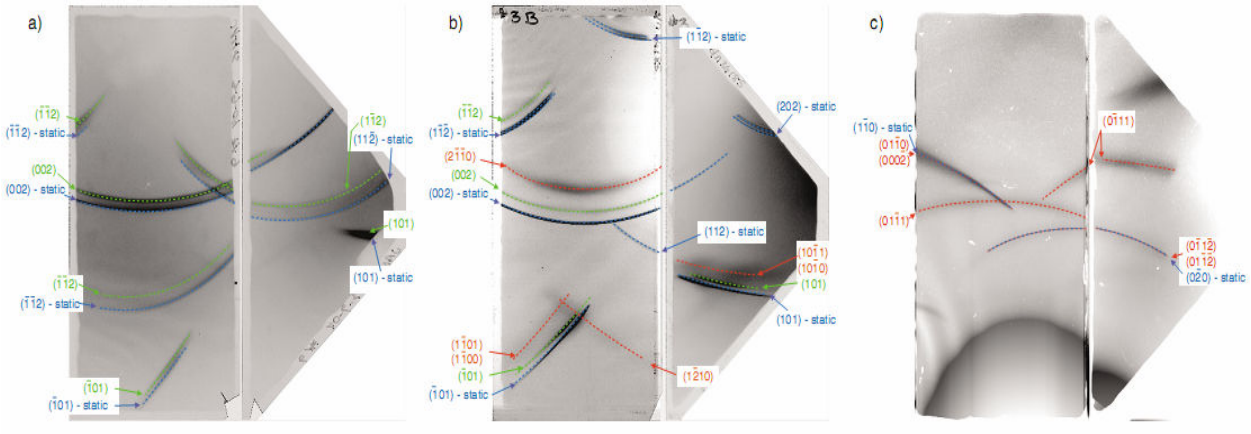

Fig. 5: Sample x-ray diffraction images in Kalantar et al. [5]: (a) reflection at low shock pressure, (b) reflection at high pressure, and (c) transmission at high pressure. The colors indicate different phases: blue- static bcc lattice, green- uniaxially compressed bcc lattice, and red- hcp phase.

The results of volume compression versus shock pressure are shown in Fig. 6. Here wavelength scaling is used to relate different experiments. The shock pressure is related to a given intensity at different wavelengths. We can see a discontinuity consistent with a volume collapse and phase transition at approximately 13 GPa. Two compressions were observed above this pressure, with the lower (open squares) for uniaxial compressed bcc lattice and the higher (solid squares) consistent with further collapse of the lattice and transition to hcp. Both compressions are shown to indicate their simultaneous presence in the measurements. The results are consistent with postprocessed NEMD simulations shown as black circles in the plot. Note that they are also consistent with the shock Hugoniot for polycrystalline iron in Boettger and Wallace [9] (solid line).

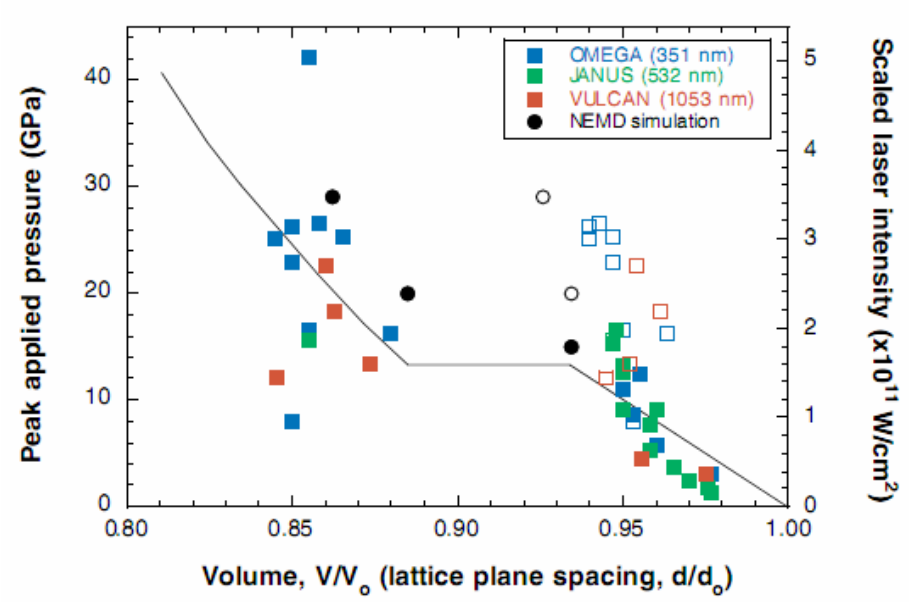

Fig. 6: Volume compression versus peak drive pressure. Solid points represent the higher compression and open points represent the lower compression for each experiment. Results from postprocessed NEMD simulations (black circles) and the shock Hugoniot (solid line) are shown overlaid.

In conclusion, we reviewed computational and experimental studies of shock-induced structural phase transitions in iron. The nanosecond *in situ* x-ray diffraction measurements confirmed the transition under shock loading and directly observed a collapse and shuffle of alternate (110) planes to form the hcp structure. The result is consistent with large-scale nonequilibrium molecular dynamics simulations, while the potential model should be modified from temperature-induced to shock-induced transitions. This work is confined to perfect single crystals, while it provides new insights into material dynamics containing plasticity, cracks and dislocations [10].

References

[1] K. Bhattacharya, *Microstructure of Martensite: Why It Forms and How It Gives Rise to the Shape-Memory Effect* Oxford University Press, New York, 2004.

[2] K. Bhattacharya, S. Conti, G. Zanzotto and J. Zimmer. *Nature* 428: 55, 2004.

[3] K. Kadau, T. C. Germann, P. S. Lomdahl, and B. L. Holian, *Science* 296: 1681, 2002.

[4] K. Kadau, T. C. Germann, P. S. Lomdahl, and B. L. Holian, *Phys. Rev. B*, 72: 064120, 2005.

[5] D. H. Kalantar *et al.*, *Phys. Rev. Lett.* 95: 075502, 2005.

[6] J. Hawreliak *et al.*, *Phys. Rev. B*, 74: 184107, 2008.

[7] J. M. Brown, J. N. Fritz, R. S. Hixson, *J. Appl. Phys.* 88: 5496, 2000.

[8] F.M. Wang and R. Ingalls, *Phys. Rev. B* 57:5647, 1998.

[9] J.C. Boettger and D.C. Wallace, *Phys. Rev. B* 55:2840, 1997.

[10] N. K. Bourne, G. T. Gray III, and J. C. F. Millett, *J Appl. Phys.* 106:091301, 2009